Draft version January 20, 2003
Preprint typeset using LaTeX style emulateapj

SLAC-PUB-9637
January 2003

SIMULTANEOUS *CHANDRA* AND *RXTE* OBSERVATIONS OF THE NEARBY BRIGHT SEYFERT 2 GALAXY NGC 4945

Chris Done
Department of Physics, University of Durham, South Rd, DH1 3LE Durham, UK
Greg M. Madejski
Stanford Linear Accelarator Center, 2575 Sand Hill Rd, Menlo Park, CA 94025, USA
Piotr T. Życki
Nicolaus Copernicus Astronomical Center, Bartycka 18, 00-716 Warsaw, Poland
Lincoln J. Greenhill
Harvard-Smithsonian Center for Astrophysics, 60 Garden St, Cambridge, MA 02138, USA

Draft version January 20, 2003

ABSTRACT

We analyze recent simultaneous*Chandra/RXTE* observations of the Seyfert 2 galaxy NGC 4945. The unprecedented spatial resolution of Chandra means we are able to separate the spectra of the nucleus, starburst and superwind regions, while the RXTE data extend the spectrum to higher energies. The extreme absorbing column of $N_H \sim 4 \times 10^{24}$ cm^{-2} means that the nucleus is only seen directly above 8–10 keV, while the lower energy spectrum from the nuclear region in *Chandra* is dominated by reflection. By contrast, the superwind is dominated by emission from hot plasma, but the starburst region contains both hot plasma and reflection signatures. To form a reflected spectrum requires that the starburst region contains clumps of cool, optically thick material, perhaps star forming cores, which are irradiated by 7–10 keV photons from the nucleus. Since photons of this energy are obscured along the line sight then this confirms the result of Madejski et al. (2000) that the extreme absorbtion material is disk-like rather than a torus. However, the IR/optical limits on the lack of high excitation emission lines show that by contrast the lower energy photons from the nucleus are obscured in all directions. We discuss the complex absorption structure revealed by these observations, and propose an an overall source geometry in which the nucleus is completely embedded in material with $N_H \sim 10^{23}$ cm^{-2}

1. INTRODUCTION

Our best current picture of Seyfert 2 galaxies relies on the Unified Scheme, where all the main ingredients of the nucleus – black hole, accretion disc and broad line region – are identical in all active galaxies, but the classification depends on the orientation with respect to the line of sight. There is a small scale, geometrically thin accretion disk around the black hole, while at distances larger than ~ 1 pc there is a geometrically thick molecular torus. The material in the disk and torus provides intrinsic obscuration, such that for the viewing directions intersecting the disk and/or torus, the intrinsic emission of the AGN is modified by the absorbing material. In particular, the light from the broad optical / UV emission lines is obscured by dust, while photoelectric absorption by gas and dust gives a low energy cutoff in the soft X–ray emission. The magnitude of the absorption depends on the column density of material in the line of sight. For columns of $N_H > 10^{25}$ cm^{-2} the central engine can be completely obscured, though some small fraction of the intrinsic nuclear light can be seen as a result of electron scattering by low density, ionized gas; this gas would be located around the axis of symmetry of the system, both within the torus and in a form of a wind emanating from the nucleus.

Such a picture is broadly consistent with a range of observed optical, X–ray, radio and polarization properties of Seyfert 1 and 2 galaxies (see e.g. the review by Veron-Cetty & Veron 2000), but these data are generally indirect as they do not resolve any of the structures proposed. One of the nearest AGN of any kind – and thus the most appropriate for a detailed study of the spatial structure to test these Unified models – is the nearby (3.7 Mpc; Mauersberger et al. 1996) Seyfert 2 galaxy NGC 4945. Spatial studies are further aided by the strong absorption, with an equivalent hydrogen column density of $\sim 4 \times 10^{24}$ cm^{-2} (Iwasawa et al. 1993; Done, Madejski, & Smith 1996; Madejski et al. 2000), corresponding to $\tau_{\rm Thomson}$ of ~ 2.4. With this column, the nuclear X-ray flux at energies corresponding to the Fe L and Kα lines is entirely absorbed, so the measured line fluxes originate in the scatterer or in the obscuring medium, yet above $\sim$ 10 keV, the nuclear power law dominates the spectrum. In fact, it is the brightest Seyfert 2 galaxy above 20 keV, as measured by OSSE (Done, Madejski, & Smith 1996), RXTE (Madejski et al. 2000), and BeppoSAX (Guainazzi et al. 2000). The hard X-ray emission is rapidly variable, on time scales of $\sim$ a day or less, implying that the Thomson-thick absorption is probably confined to a structure which is geometrically rather thin, i.e. more probably associated with the disk rather than the torus (Madejski et al. 2000). Importantly, NGC 4945 is an H_2O megamaser source (Dos Santos & Lepine 1979), which traces underlying cool, dense molecular structures probably within ~ 1 pc of the central engine. Unlike NGC 4258, this emission does not give the smooth rotation curve expected from a well ordered disk, but assuming this irregular, clumpy distribution still traces orbital motion gives an estimate of the central mass of $\sim 1.4 \times 10^6$ M$_\odot$ (Greenhill, Moran, & Herrnstein 1997).

* Work supported in part by the Department of Energy contract DE-AC03-76SF00515.

Knowing the intrinsic X–ray luminosity *and* the mass of the central source allows an estimate of the accretion rate in Eddington units of 10% (Greenhill et al. 1997; Madejski et al. 2000), and aids in detailed dynamical studies of the source.

The ionized material filling the opening of the torus also emits recombination line and continuum radiation, generally resulting in strong Fe L and Kα lines (Krolik & Kallman 1987; Band et al. 1990). However, despite this theoretical work there is comparatively little known about the scattering region in Seyfert 2s. This is mainly due to spatial confusion, as Seyfert nuclei often co–exist with nuclear starbursts/superwind activity, and these contribute to the soft X–ray emission and Fe L lines. This is certainly the case for NGC 4945 (Heckman, Armus, & Miley 1990; Nakai 1989). To disentangle the effects of the scattering region from the starburst and superwind, we need high spatial resolution, provided by the superior angular resolution available with *Chandra*.

In this Paper, we report on the *Chandra* imaging observations of the nuclear region of NGC 4945. These have already been published by Schurch, Roberts & Warwick (2002), but here we do a much more detailed spatially resolved analysis. We also include simultaneous data from RXTE in order to constrain the direct nuclear spectrum, and present a plausible interpretation regarding the geometry of the source which fits with both the IR/optical and X-ray constraints.

2. OBSERVATIONS

2.1. *Chandra*

The *Chandra* data were taken on 27 - 28th January 2000 with the ACIS camera in the faint mode for a total of 49 ks, with the nucleus focussed on the S3 chip. The filtered file produced by standard processing was further cleaned by running the software tool `acisscreen` and gain corrected using `acisgaincorr`. These cleaned data from the chip S3 were screened to reject periods of high background (defined as times at which the total count rate of events labelled as valid was greater than 20 counts per second), and the resulting image of NGC 4945 with exposure of 38 ks is shown in Fig. 1. The image clearly shows a point-like emission coincident with the megamaser source, and diffuse "plume" extending roughly in the NW direction from the nucleus, which is perpendicular to the plane defined by the megamaser emission of the galaxy, which in turn is closely aligned with the plane of the host galaxy. We perform spectral analysis of various regions of that image separately as described below.

The nuclear spectrum (hereafter called `nuc`) was extracted from a circle of radius 4 pixels (2 arcsec) centered on the brightest spot. The nearby diffuse emission was taken from a box surrounding this region, excluding a circle of radius 4.5 pixels centered on the nucleus (hereafter called `diff-nuc`). Further diffuse emission spectra were taken from two regions shown overlaid on Fig. 1, hereafter called `diff-1` and `diff-2`. A background spectrum was taken from a nearby, source free region. The response and auxiliary files were created for the nuclear region using `acismakermf`, `acisarfprep` and `mkarf`, and these files were used for all spectra. For the subsequent analysis, we grouped all extracted spectra such that there were at least 20 total counts per new bin.

2.2. *RXTE PCA and HEXTE*

The simultaneous RXTE data were extracted using the rex script, with the Epoch 4 faint source background models. This resulted in a total of 60 ks of PCA data from layer 1, detectors 0 and 2. As in the previous RXTE observations of this object, the source counting rate is rather modest, with source counts being less than 10 per cent of background.

We know from previous observations that the nucleus of NGC 4945 is a relatively hard X-ray source, where the primary, nuclear emission can be well described as a heavily absorbed power law. Since we are mainly interested in the RXTE PCA data regarding the nuclear component, we present the PCA lightcurve in the 8–30 keV band (channels 19 - 69) in Fig. 2, with contiguous orbits giving even sampling of the lightcurves on timescales of a few thousand seconds, spanning a total of ~ 1.5 days. This extends the variability seen in the previous monitoring campaign, which had single orbit snapshots once per day for ~ 1.5 months (Madejski et al. 2000). Plainly there is considerable variability power in this object on timescales shorter than 1 day.

The HEXTE data from clusters 0 and 1 were also extracted with the rex script, and here the background is even more dominant. Nonetheless, the variability seen in the PCA and HEXTE are consistent with each other (Figure 3). Since the method of background estimation is very different in the PCA (blank field predictions) and HEXTE (offset pointings) then this shows that the majority of the variability seen is indeed connected to the source rather than to background uncertainties. We use the HEXTE data from 20–100 keV, and allow for a normalisation offset between this and the PCA.

3. NUCLEAR SPECTRUM

3.1. *Chandra*

The superb imaging capabilities of *Chandra* allow an extraction of the spectrum from the nuclear source alone. This is shown in Fig 4 and is clearly dominated by iron Kα line emission, but also includes a hard broad-band continuum. We fit this with an absorbed power law and iron line and find that the nuclear continuum is indeed extremely hard, with $\Gamma = -0.9$, and that the (narrow, σ fixed at 10 eV) line at 6.4 keV has a large equivalent width of 1.3 keV ($\chi^2_\nu = 66.0/51$).

The fit can be significantly improved if the line is broad, or if it consists of a number of components. Allowing the line to be broad we obtain $\chi^2_\nu = 47.9/50$ with $\sigma = 0.09^{+0.09}_{-0.03}$ keV, and the EW increases to 2 keV with intensity $2.0 \pm 0.4 \times 10^{-5}$ photons s^{-1}. Alternatively, adding a second, narrow line at 6.5 keV (fixed energy) gives $\chi^2 = 48.3/50$ and EW of 570 eV and 270 eV for the 6.4 and 6.5 keV components, respectively. Repeating the fits to ungrouped data, using C-statistics, gives (for 1043 PHA bins): C-stat=929 for a narrow Gaussian at 6.38 keV, C-stat=906 for a broad Gaussian and C-stat=911 for two narrow Gaussians. There is thus a preference for a broad line, but it is rather marginal.

Clearly, the very hard power law component cannot be the nuclear continuum observed directly. Instead, in an

attempt to construct a more physical model of the source, we interpret the spectrum of the compact region in the *Chandra* data to be solely due to Compton reflection of an unseen primary continuum. With this physical model we obtain $\chi^2_\nu = 65.2/53$ for reflection of an intrinsic (unseen) power law of $\Gamma = 1.35^{+0.26}_{-0.22}$ by neutral, solar abundance material (assumed inclination of 60°). The line emission in this model is calculated self-consistently with the reflected continuum (Życki, Done & Smith 1999), so its equivalent width is fixed with respect to the reflected continuum for a given illuminating power law and reflector ionization state and inclination ($\sim$ 1.4 keV for the parameters used here). The model also includes the Compton downscattered shoulder on the iron K line, so the line is intrinsically broad. However, the fit can be significantly improved ($\chi^2_\nu = 56.3/52$) by allowing the spectral features to be further broadened, corresponding to a radius of $\sim 10^3\,R_g$ if this is from Keplerian motion.

The deconvolved spectrum with the unsmeared reflection model is shown in Fig. 4. There is a marginally significant residual ($\Delta\chi^2 = 5$ for 2 additional degrees of freedom) for a narrow line at energy 6.73 ± 0.08 which could indicate the presence of reflection from more highly ionised material.

3.2. *Broad-band nuclear spectrum*

Fig. 5 shows the broad band nuclear spectrum derived from fitting the nuclear spectrum from *Chandra*, together with the PCA and HEXTE data. *Chandra* can spatially resolve the nuclear emission in the 1–10 keV range, but both the PCA and HEXTE data cover a large field of view ($\sim 1 \times 1$ degree), so include a contribution from off–nuclear point sources and host galaxy diffuse emission as well as the nucleus itself. We fit the spectra from the 3 instruments simultaneously, but include a contribution from extended emission in the PCA and HEXTE spectra which is set to zero in the *Chandra* data. This extended emission can be well fit by a hot plasma (modelled here using a solar abundance MEKAL code), and we also include an additional emission line at 6.4 keV. The nuclear emission is modelled by a heavily absorbed power law and its weakly absorbed reflection (PEXRAV plus a gaussian line), and results are detailed in Table 3.2. The overall shape of the spectrum is very similar to that seen in previous observations, and a direct comparison of the PCA spectrum with that of Madejski et al. (2000) shows no evidence for any changes in spectral shape, but the absorbed power law emission from the nucleus is a factor 1.8× brighter in the observations reported here.

The PCA spectrum contains much more line emission than seen in Chandra. While much of this is consistent with moderately ionised (6.5–6.7 keV) emission from the hot diffuse plasma, there is also evidence for some additional line at 6.4 keV, impling a contribution to the fluorescent emission from the extended region (see also Guainazzi et al. 2000; Schurch et al. 2002 and Section 4 below).

The heavy absorption towards the nucleus implies that the obscuring material is optically thick to electron scattering, with an optical depth of a few. This scattering changes the spectral shape from that obtained by pure absorption, and we model this using the Monte Carlo code of Krolik, Madau & Życki (1994). Motivated by previous and current observations where the rapid variability implies a rather geometrically thin (disk-like) absorbing structure, we assume that the absorbing material subtends a rather small solid angle to the X-ray source (Madejski et al. 2000). We assume this material forms a symmetric torus, with half-angle of the absorber as seen from the central source of 10° i.e. a torus opening angle of 80° which we view at 90° (see Madejski et al. 2000). We also replace the separate reflection continuum/line model used above with the self consistent reflected spectrum model. This fit is detailed in Table 3.2, and the resulting unfolded spectrum is plotted in Fig. 5. The overall spectral index is $\Gamma \sim 1.8$ with confidence contours on the spectral index and optical depth of the absorber are plotted in Fig. 6.

The optically thick absorption means that the true power law intensity is suppressed by a factor $\sim exp(-\tau)$ even at 50-100 keV. The inferred power law normalisation corrected for this large (but fairly uncertain, see Fig. 6) factor gives a 0.1-200 keV flux of 4.5×10^{-8} ergs cm^{-2} s^{-1}. This implies an intrinsic X-ray flux of 7×10^{43} ergs cm^{-2} s^{-2} in the 0.1–200 keV bandpass, which is 50 per cent of the Eddington limit and similar to the observed FIR luminosity. Thus it is likely that the AGN powers a substantial fraction of the observed FIR emission (Marconi et al. 2000).

3.3. *Origin of the nuclear 6.4 keV Fe K line*

Clearly, one of the main questions is the origin of the Fe K line. In the model of the nuclear spectrum above the line can arise either in the reflector or in the optically thick absorbing material. This distinction may be somewhat artificial as its possible to envisage a geometry in which the absorber and reflector are the same structure, e.g. where we are looking at an absorbing disk at an angle closer to 80° (the assumed opening angle) rather than 90° so reflected photons from the far side of the disk can be seen without being absorbed. Any warp on the disk will also enhance the solid angle of reflecting material which can be seen, and it is noteworthy that the maser emission in this and other AGN indicate that the cool material at 0.1–1 pc has a shallow warp.

In our assumed geometry, where we view the absorbing disk/torus at 90° then this material produces $\sim$ 25% of the total line seen from the nucleus. The separate reflecting material produces the rest of the line, and for solar abundances, the equivalent width of the line to reflected continuum is about 1.3–1.6 keV (George & Fabian 1991; Matt, Perola & Piro 1991). This is not strongly affected by increasing the abundances of all the heavy elements - this increases the amount of line produced, but also increases the opacity so fewer line photons escape (George & Fabian 1991). However, increasing the iron abundance relative to the other elements can give a marked change in the line equivalent width (George & Fabian 1991), and fits to the *Chandra*/*RXTE* full nuclear continuum using absorption/reflection models with iron alone at twice solar abundance give a significantly worse fit than solar abundances. Iron overabundances are predicted in most chemical evolution models for AGN, and are often observed (Haman & Ferland 1993). However, there is a delay of $\sim 1-2$ Gyrs for the onset of the Fe producing Type 1a supernovae, so our observed solar abundances are consistent with models for a young starburst (0.01 Gyr) in this object (Marconi

TABLE 1
RESULTS OF MODELING THE NUCLEAR SPECTRUM FROM CHANDRA, PCA AND HEXTE SIMULTANEOUS DATA

N_H[a]	Γ	Norm	N_H[b]	f_{refl}[c]	Fe Kα intensity[d]	χ^2/dof
425 ± 25	1.65 ± 0.15	0.03	$0.8 \pm 0.8^{+1.2}_{-0.8}$	$6 \pm 2 \times 10^{-2}$	$2.0+0.5_{-0.3} \times 10^{-5}$	105.5/111[e]

[a]Absorption applied to the intrinsic nuclear (power law) spectrum in units of 10^{22} cm^{-2}

[b]Absorption applied to all spectral components in units of 10^{22} cm^{-2}

[c]Solid angle subtended by the reflector (i.e. normalization relative to the direct power law normalization) in units of $\Omega/2\pi$. Assumes a reflector inclination of 60°.

[d]6.4 keV iron line emission from the nucleus in photons cm^{-2} s^{-1}

[e]There is also a mekal plasma ($kT = 5.3^{+2.0}_{-1.1}$ keV, 2–10 keV unabsorbed flux of 5×10^{-12} ergs s^{-1}) and additional 6.4 keV narrow gaussian line with intensity $2.0 \pm 0.9 \times 10^{-5}$ photons cm^{-2} s^{-1} in the PCA and HEXTE data (normalizations set to zero in Chandra) so as to account for the extended emission in their wide fields of view.

et al. 2000).

Our reflection model assumes that the iron line is produced in optically thick material. However, the line equivalent width can also be affected by the column density of the material. The reflection models assume that the material is optically thick, i.e. $N_H \geq 2 \times 10^{24}$ cm^{-2}. At these columns then all the photons above the iron edge which can produce the fluorescence line are absorbed. If the column is reduced below $\sim 10^{23}$ cm^{-2} then this is no longer true. The material becomes thin to the photoelectric absorption opacity at the iron edge and the line decreases. But this also changes the reflected continuum - depending on the geometry it can either look like a standard reflection spectrum up to the point where the material becomes optically thin to photoelectric opacity or it can look like straightforward absorption by a column of 10^{23} cm^{-2}. Given that the observed *continuum* in *Chandra* looks like optically thick reflection up to at least 6-7 keV then the column density of the reflecting material *must* be at least 10^{23} cm^{-2}.

4. DIFFUSE EMISSION

The *Chandra* spectra from the diffuse emission regions extracted from regions located at progressively further distances from the nucleus are shown in Fig. 7. The nuclear spectrum itself is shown for comparison in the top panel. Plainly the diffuse spectra nearby the nucleus (`diff-nuc` and `diff-1`) contain a substantial iron Kα line and show a hard continuum spectrum, which suggests that they are also dominated by Compton reflection from optically thick material at high energies. However, the increasing counts at low energy, and increasing strength of line features (such as the $\sim$ 1.8 keV line, presumably due to He–like silicon, and the iron L emission lines) show that there is also an increasing fraction of the emission from hot/photoionized plasma as distance from the nucleus increases. This hot plasma could be either predominantly photoionised by the nucleus, or mechanically heated by the starburst. In either case it will contain some free electrons which scatter some fraction of the nuclear light, giving an additional scattered power law component.

We assume the intrinsic primary emission is an isotropically emitted power law with fixed index 1.85 and normalisation of 2.79 photons cm^{-2} s^{-1} at 1 keV, as derived from Section 3.2. Some fraction, f_{refl} of this is reflected from cold material (again we use the reflection code in which the self-consistent iron line emission is included), while another fraction, f_{scatt} is scattered from hot electrons, forming a power law.

We first assume that the line emission is from a mechanically heated plasma (using the MEKAL code), and these fits are detailed in Table 4. We also include fits to the *Chandra* nuclear spectrum, to show the limits on the scattered and hot gas emission on the smallest scales, though here we truncate the data at 6.6 keV so as not to include any transmitted flux. With this different energy range the line broadening is much less significant, at $\Delta\chi^2 = 3$.

The data show clear differences in the absorping column, decreasing as a function of distance from the nucleus. The ISM in our galaxy in this direction has $N_H \sim 2 \times 10^{21}$ cm^{-2} while the observed column is significantly higher than this in all fields except `diff-2`. This is unsurprising as NGC 4945 is an edge on galaxy. The *Chandra* nuclear spectrum is inferred to be $\sim 5\times$ more absorbed in these fits than from the reflection model fitting in Section 3.1. This is due both to the steeper illuminating spectrum and to ignoring the data above 6.6 keV which include some component from the direct nuclear emission. Intruiguingly, CO observations imply a ring of molecular gas with column of $\sim 7 \times 10^{22}$ cm^{-2} in the nuclear direction (Whiteoak et al. 1990), and photoelectric absorption is known to follow the molecular gas column in Seyfert 2's (e.g. Wilson et al. 1998).

The data also indicate that the different spectral components behave differently with distance from the nucleus. The neutral reflected fraction is highest in the nu-

TABLE 2
RESULTS OF MODELING THE DIFFUSE EMISSION DATA WITH THE MEKAL MODEL

file	N_H $\times 10^{22}$ cm^{-2}[a]	kT (keV)	mekal flux ergs s^{-1}[b]	f_{scatt}[c]	f_{refl}[d]	χ^2/dof
`nuc`	$7.1^{2.9}_{-3.5}$	0.7[e]	$2.4^{+4.5}_{-2.4} \times 10^{-12}$	$0^{+0.8} \times 10^{-5}$	$1.2^{+0.2}_{-0.1} \times 10^{-3}$	51.6/43
`diff-nuc`	$3.8^{+1.3}_{1.2}$	0.7[e]	$3.4^{+9.6}_{-3.4} \times 10^{-13}$	$1.8^{+0.7}_{-0.6} \times 10^{-5}$	$4.1 \pm 1.1 \times 10^{-4}$	35.8/39
`diff-1`	1.8 ± 0.2	0.71 ± 0.11	$1.0^{+0.4}_{-0.7} \times 10^{-12}$	$3.4^{+4.6}_{-3.4} \times 10^{-6}$	$4.5^{+0.5}_{-0.9} \times 10^{-4}$	62.5/62
`diff-2`	$0.32^{+1.1}_{-0.7}$	0.68 ± 0.08	$1.0^{+0.5}_{-0.3} \times 10^{-13}$	$5.1 \pm 1.2 \times 10^{-6}$	$6.5^{+400}_{-6.5} \times 10^{-7}$	60.2/76

[a] Foreground absorption applied to all model components

[b] Bolometric, unabsorbed flux extrapolated over 0.01–100 keV

[c] Normalization relative to that of the primary known from the broad band modeling.

[d] Normalization in units of $\Omega/(2\pi)$. Assumes inclination 60°.

[e] Temperature fixed at 0.7 keV as the component is not significantly detected.

cleus, then is smaller in `diff-nuc` and `diff-1`, and much smaller (not significantly detected) in `diff-2`. Conversely, the medium energy emission component modelled here as scattered nuclear flux is not significantly detected in the nucleus, is largest in `diff-nuc` and `diff-1`, while it is smaller but still significant in `diff-2`. The low energy, warm gas component is not significantly detected in `nuc` or `diff-nuc`, but has a total luminosity of $\sim 10^{39}$ and $\sim 10^{38}$ ergs s^{-1} in `diff-1` and `diff-2`, respectively. The fits are acceptable in all cases, although line-like residuals remain in `diff-nuc` and `diff-1`.

The self-consistency of this model can be checked by estimating the density of the mekal plasma diffuse emission, and then using this to calculate how important photo-ionisation should be. The luminosity of a mekal plasma of density n in volume V is $\Lambda n^2 V$, where $\Lambda \sim 3 \times 10^{-23}$ ergs cm^{-3} s^{-1} for a temperature of ~ 1 keV. The three regions, `diff-nuc`, `diff-1` and `diff-2`, have volume of $\sim 5 \times 10^{61}$, 7×10^{61} and 10^{63} cm^3, respectively (assuming axial symmetry), so the hot plasma densities are $\sim 1.7, 0.5$ and 0.07 cm^{-3} assuming it smoothly fills the volume. In our model this hot gas also scatters the direct nuclear flux. The scattered fraction $f_{scatt} = \Omega/(4\pi)\tau = \Omega/(4\pi) n \sigma_T \Delta r$, where the solid angle $\Omega/4\pi \sim 1, 0.27$ and 0.16 for `diff-nuc`, `diff-1` and `diff-2`, and the path length $\Delta r \sim 30, 86$ and 350 pc. The scattered fraction predicted by the hot plasma is $\sim 10^{-4}, 2.3 \times 10^{-5}$ and 8×10^{-6}. These are significantly bigger than the scattered fractions derived from the fits, except for `diff-2`. The fit result scattered fractions predict densities of $\sim 0.3, 0.05$ and 0.06 cm^{-3}, respectively, for plasma smoothly filling the volume.

The distance r from the nucleus in each case is $\sim 50, 93$ and 230 pc, so the ionisation parameter, $\xi = L/(nr^2)$, is approximately constant at ~ 2000 in each region. This high value indicates that the model of collisionally heated hot gas filling the volume is *not* self-consistent. Either the gas is strongly clumped, so that its density is higher by a factor of > 10, or photoionisation will dominate over collisional equilibrium. A key problem with having photo-ionisation dominate is that there are *no* signatures of the AGN illuminating the extended emission in any other waveband. There are *no* standard AGN high excitation narrow lines in the optical (e.g. [OIII] Moorwood et al. 1996), near- or mid-IR (Genzel et al. 1998; Marconi et al. 2000: Spoon et al. 2000), and the [FeII]/Brγ line ratios are indicative of shock heating rather than photoionisation (Reunanen, Kotilainen & Prieto 2002). The observed extended emission line regions *must* be shielded from the nuclear photoionising flux (5 eV–1 keV: Marconi et al. 2000), but the extended 6.4 keV line emission shows that it *must* be illuminated by photons ≥ 7 keV. Hence the nucleus must be absorbed by columns of $\geq 10^{22}$ cm^{-2} in *all* directions.

Photo-ionisation by such a hard (absorbed) X-ray spectrum would lead to fluorescence lines from mostly neutral material rather than ionized line emission. This is observed in the extended 6.4 keV Fe line emission (significantly detected in `diff-nuc` and `diff-1`), but this cannot explain the lower energy line emission (e.g. Si at 1.8 keV or the iron L complex in `diff-1` and `diff-2`). Thus the low energy lines must be from collisionally ionised material, so the mekal parameters derived above indicate that the material *must* be clumpy.

The requirement that the nuclear spectrum be absorbed means that the model of a power law for the scattered flux is also not consistent. Replacing this by an *absorbed* power law gives stringent constraints in `diff-2`. Absorption of $N_H \sim 1.4 \times 10^{21}$ on the scattered flux increases χ^2 by 2.7, while columns of 10^{22} and 10^{23} cm^{-2} increase it by 8.5 and 12.5, respectively. Thus it seems most likely that the 3–5 keV continuum is *not* from scattered nuclear flux but rather is from hot, clumped gas.

Models of starburst galaxies indicate that the material is indeed strongly clumped (Suchkov et al. 1996; Strickland & Stevens 2000), such that multiphase and multitemperature gas exists at all radii. We replace the scattered component with a second, higher temperature mekal plasma. This gives similar χ^2 fits to all the spectra, but requires

temperatures of 4–7 keV in addition to the lower temperature gas at 0.5–0.7 keV. Such hot gas is difficult to produce (Suchkov et al. 1994; Strickland & Stevens 2000), but this component is observed in pure starburst galaxies (Pietsch et al. 2001), and a similar model with multitemperature hot components was used by Schurch et al. (2002) to fit the diffuse emission in both *Chandra* and *XMM*. An alternative explanation could be that it is from an unresolved population of X-ray binaries (Persic & Rephaeli 2002).

To summarize, *all* the off nuclear spectra require that the gas is multiphase. The most likely interpretation is that they all have multitemperature clumps of hot gas, while `diff-nuc` and `diff-1` also strongly require the presence of cool, optically thick clumps.

5. THE OVERALL GEOMETRY

The *Chandra* image can be superimposed on previous images of this galaxy at other wavelengths. Our `diff-nuc` spectrum corresponds to the 100-200 pc edge-on starburst ring traced by molecular gas (Br γ: Moorwood et al. 1996, Pa α and H_2: Marconi et al. 2000 and CO: Curran et al. 2001). This ring has its major axis along the major axis of the host galaxy (NE-SW direction), which also matches the position angle of the central maser disk (Greenhill et al. 1997).

The `diff-1` spectrum extends into the region of molecular gas where the emission is dominated by H_2 rather than by Paα (Marconi et al. 2000). The Paα line traces mainly starburst activity, while the H_2 emission probably reflects shock heating on the edges of the superwind cone (Moorwood et al. 1996). The `diff-2` spectrum covers the extended narrow line emission seen as a cone in the low excitation lines Hα and [NII] (Moorwood et al. 1996).

The extreme absorption seen towards the nucleus in X-rays corresponds to optical depths of $\sim$ 2.5 to electron scattering. This material has a rather small scale height as otherwise the scattered X-rays would noticeably smear the hard X-ray variability (Madejski et al. 2000). A small, dense inner disk is also required to produce the observed maser emission, so we identify the extreme absorber with the masing disk. This material is distributed over a patch $\sim 0.7 \times 0.1$ pc in size (Greenhill et al. 1997), representing H_2 densities on the order of 10^8 to 10^{10} cm^{-3} for fractional H_2O abundances of 10^{-4} to 10^{-5} (Elitzurm 1992), so giving a potential column of $N_H > 10^{26}$ cm^{-2}. Since this is considerably bigger than the observed obscuration then we may not be in the maximally absorbed, completely edge-on, line of sight.

In addition to the dense absorbing disk, the central engine must be completely embedded in obscuring material within $\sim$ 25 pc so that UV and soft X-ray fluxes do not escape (Marconi et al. 2000). Although this additional absorption could be associated with material from the starburst-related inflow along a bar (Ott et al. 2001), we suggest that it may be a high latitude extension of the dense absorber (i.e., the maser-emitting material is a thickening in the equatorial plane). As such the central parsec of NGC 4945 could be more gas rich than that for most other Seyfert galaxies. In this sense, NGC 4945 may be similar to NGC 3079, another active galaxy that exhibits very large columns (Iyomoto etal. 2001), substantial nuclear star formation (Cecil et al. 2001 and references therein), and a disordered but otherwise disk-like distribution of H_2O masers (Trotter et al. 1998). This absorber is probably seen in the column of $N_H \sim 7 \times 10^{22}$ cm^{-2} inferred on the reflected nuclear X-ray spectrum, corresponding to $A_v \sim 35$. This is also the absorbing column seen to the far IR nuclear source (Krabbe et al. 2001).

On much larger scales there is absorption associated with dusty nuclear starburst ring which forms a $\sim$ 100-200 pc torus around the nucleus (Marconi et al. 2000). This picture fits into the growing evidence for two distinct absorption structures in many AGN, with a compact, extreme absorption region surrounded by an extended dusty lower absorption region (e.g. Granato et al. 1997).

The energy from supernovae in the starburst ring produces hot multiphase gas which emits in the soft X-ray range. A population of X-ray binaries may also contribute to the spectrum from this region, which would remove the requirement for some of this gas to be as hot as $\sim$ 6 keV. However, flux at $\sim 3-4$ keV is also required in the superwind (`diff-2`) region, where it is hard to envisage anything other than hot gas being present. This intrinsic diffuse emission is augmented by some scattering of the absorbed nuclear flux in cold, optically thick material. These cool clumps most probably represent starforming cores as these have density $n \sim 10^6$ cm^{-3} and size scales of 1 pc (Plume et al. 1997).

6. CONCLUSIONS

The unsurpassed X-ray imaging ability of the *Chandra* satellite allows us to disentangle the AGN and starburst/superwind contributions in NGC 4945. *Chandra* sees the nucleus only in reflection: simultaneous *RXTE* data show the direct nuclear flux absorbed by an extreme column of $\sim 4 \times 10^{24}$ cm^{-2}.

The starburst/superwind gas is clearly multi-phase, with cool clumps (seen in reflection and iron fluorescence line emission at 6.4 keV) co-existing with hot gas. The hot gas is itself clumped rather than being uniform, as otherwise it would be strongly photo-ionised in conflict with the observed spectrum from the furthest region (`diff-2`). We show that the self-consistent scattered emission from the hot gas is probably unimportant compared to its diffuse emission.

The extreme absorption of $N_H > 10^{24}$ cm^{-2} seen towards the nucleus cannot completely cover the source in all direction as the extended 6.4 keV fluorescence line emission clearly shows that the hard X-rays (7-10 keV) from the AGN illuminate the starburst ring. However, the lack of optical/IR high excitation lines from this region equally clearly shows that the UV/soft X-rays from the AGN do not illuminate this material. Either the AGN does not produce UV/soft X-rays (which seems highly unlikely) or they are absorbed in *all* directions which requires columns of $N_H > 10^{21-22}$ cm^{-2} This implies that the nucleus is completely embedded in a column of $\sim 10^{22-23}$ cm^{-2}, probably associated with molecular gas driven into the nucleus by the starburst/superwind.

7. ACKNOWLEDGEMENTS

This work was supported by *Chandra* grant from NASA to Stanford University via the SAO award no. GO0-1038A and in part by Polish KBN grant 2P03D01718. PTZ and CD thank SLAC for the hospitality during visits there.

REFERENCES

Band, D., Klein, R., Castor, J., & Nash, J. 1990, ApJ, 362, 90
Curran S. J., Johansson L. E. B., Bergman P., Heikkilä A., Aalto S., 2001, A&A, 367, 457
Done, C., Madejski, G., & Smith, D. 1996, ApJ, 463, L63
Dos Santos, P. M., & Lepine, J. R. D. 1979, Nature, 278, 34
Genzel R., et al. 1998, ApJ 498, 579
George I. M., Fabian A. C., 1991, MNRAS, 249, 352
Granato G. L., Danese L., Franceschini A., 1997, ApJ, 486, 147
Greenhill, L. J., Moran, J. M., & Herrnstein, J. R. 1997, ApJ, 481, L23
Guainazzi, M., Matt, G., Brandt, W. N., Antonelli, L. A., Barr, P., & Bassani, L. 2000, A&A, 356, 463
Heckman, T., Armus, L., & Miley, G. 1990, ApJS, 74, 833
Hamann F., & Ferland G., 1993, ApJ., 418, 11
Iwasawa, K., et al. 1993, ApJ, 409, 155
Krabbe A., Böker T., Maiolino R., ApJ, 557, 626
Krolik J. H., Kallman T. R., 1987, ApJ, 320, L5
Krolik, J. H., Madau, P., & Życki, P. T. 1994, ApJ, 420, L57
Madejski, G. M., Życki, P. T., Done, C., Valinia, A., Blanco, P., Rothschild, R., & Turek, B. 2000, ApJ, 535, L87
Marconi A., Oliva E., van der Werf P. P., Maiolino R., Schreier E. J., Macchetto F., Moorwood A. F. M., 2000, A&A, 357, 24
Matt G., Perola G., Piro L., 1991, A&A, 247, 25
Mauersberger, R., Henkel, C., Whiteoak, J., Chin, Y.-N., & Tieftrunk, A. 1996, A&A, 309, 705
Moorwood A.F.M., van der Werf P.P., Kotilainen J.K., Marconi A., Oliva E., 1996, A&A, 308, L1
Nakai, N. 1989, PASJ, 41, 1107
Ott M., Whiteoak J. B., Henkel C., Wielebinski R., 2001, A&A, 372, 463
Persic M., Rephaeli Y., 2002, A&A, 382, 843
Pietsch W. et al. 2001, A&A 365, L174
Plume R., Jaffe D. T., Evans, N. J., Martin-Pintado J., Gomez-Gonzalez J., 1997, ApJ, 476, 730
Reunanen J., Kotilainen J. K., Prieto M. A., 2002, MNRAS, 331, 154
Sambruna, R., et al. 2001, ApJ, 546, L13
Schurch N. J., Roberts T. P., Warwick R. S., 2002, MNRAS, 335, 241
Spoon H. W. W., Koornneef J., Moorwood A. F. M., Lutz D., Tielens A. G. G. M., 2000, A&A, 357, 898
Strickland D. K., Stevens I. R., 2000, MNRAS, 314, 511
Suchkov A. A., Balsara D. S., Heckman T. H., Leitherer C, 1994, ApJ, 430, 511
Suchkov A. A., Berman V. G., Heckman T. M., Balsara D. S., 1996, ApJ, 463, 528
Veron-Cetty M.P., Veron P., 2000, A&AR, 10, 81
Whiteoak J. B., Dahlem M., Wielebinski R., Harnett J. I., 1990, A&A, 231, 25
Wilson A. S., et al. 1998, ApJ, 505, 587
Życki P. T., Done C., Smith D. A., 1999, MNRAS, 305, 231

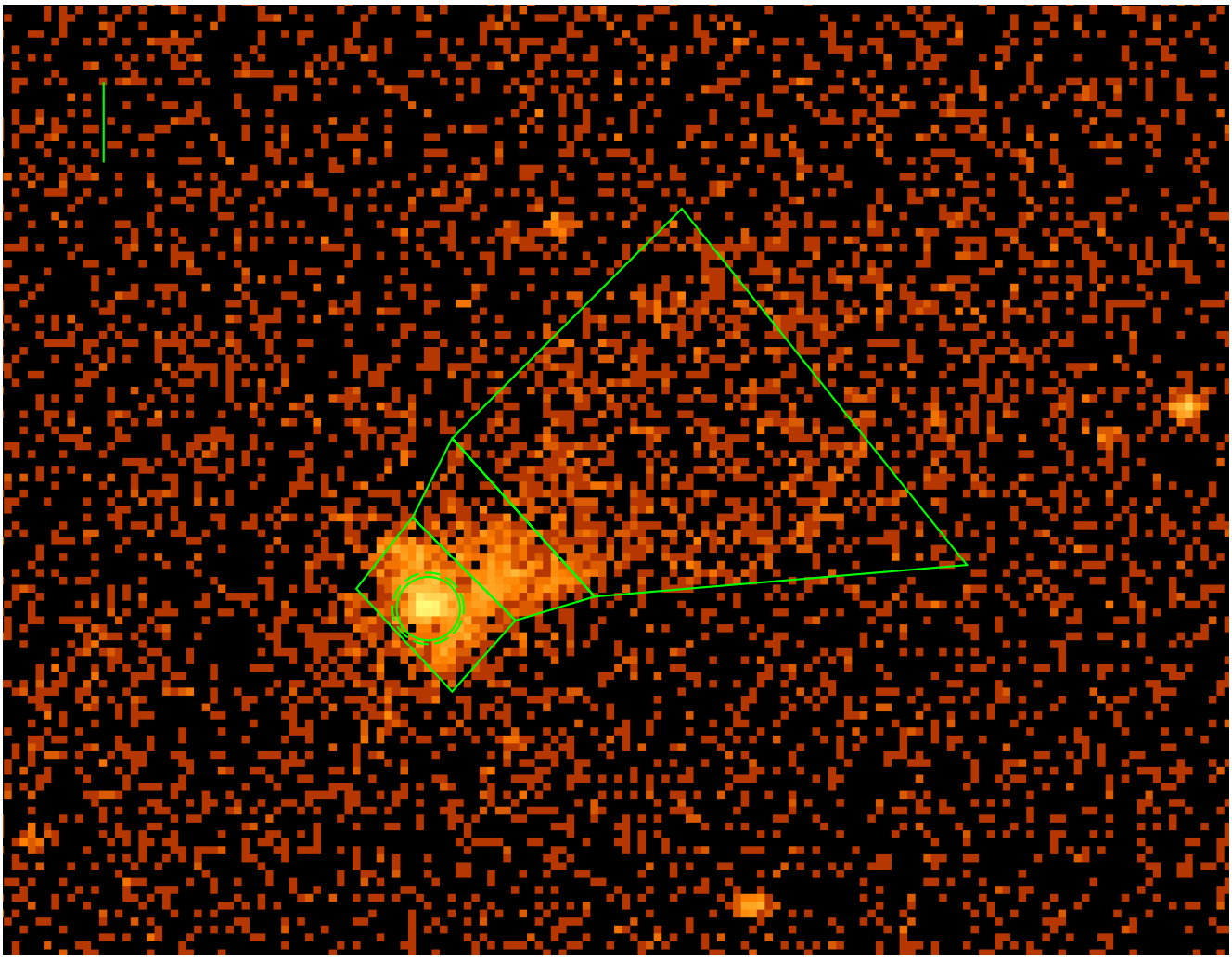

FIG. 1.— Chandra image of NGC 4945, with the spatial regions marked where the data for spectral analysis was extracted. North is up and East is to the left. The bar in the top left hand corner is 5 arcsec long (corresponding to 90 pc at 3.7 Mpc). `Nuc` is the circle centered on the nucleus, `diff-nuc` is the region surrounding this, `diff-1` is the next region to the NW, and `diff-2` is the largest region.

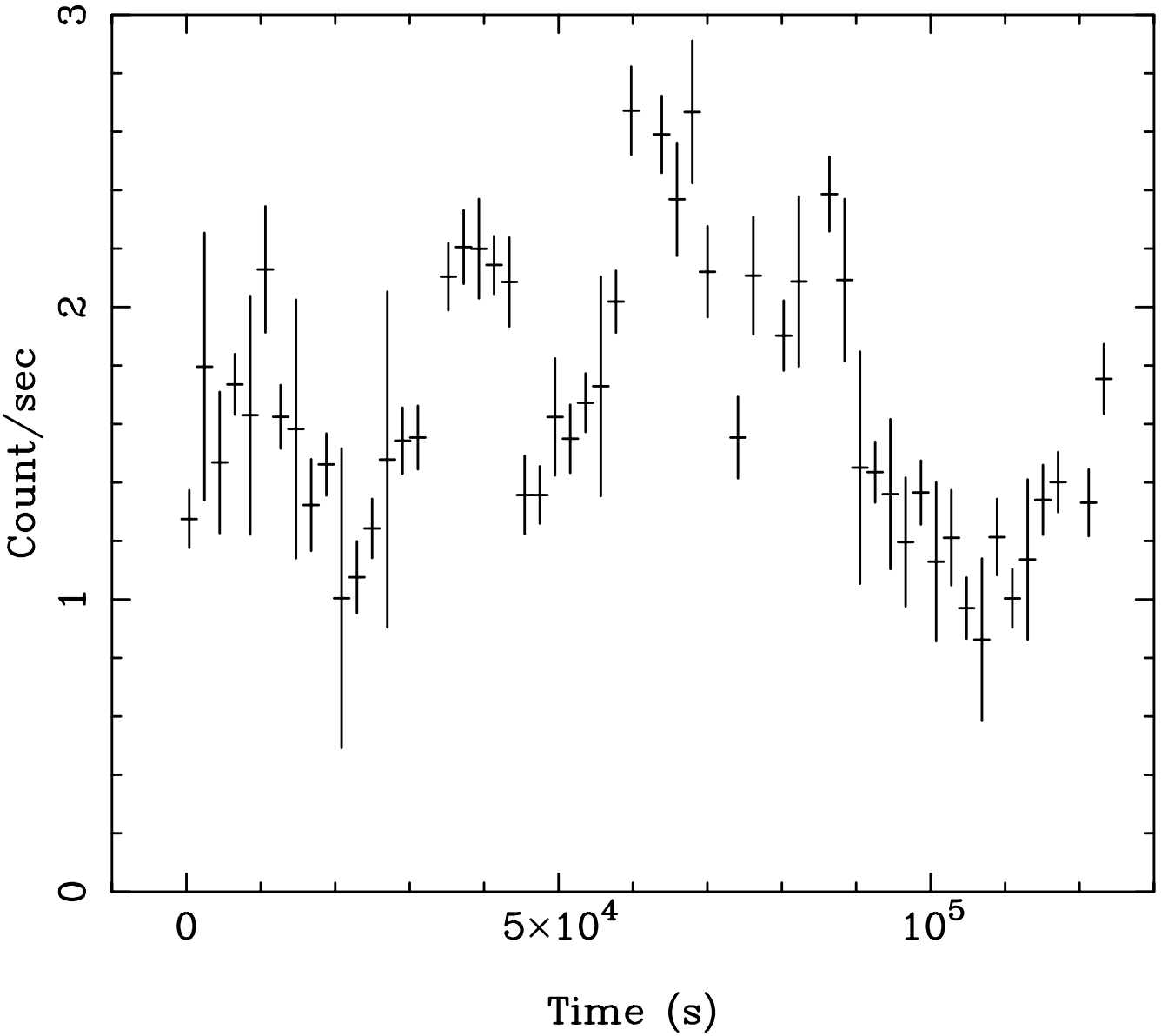

FIG. 2.— PCA 8–30 keV lightcurve (channels 19-69), binned on 4096 second intervals. Continual variability is seen, showing that the optically thick absorber cannot have a large scale height as electron scattering would then smear out the rapid changes.

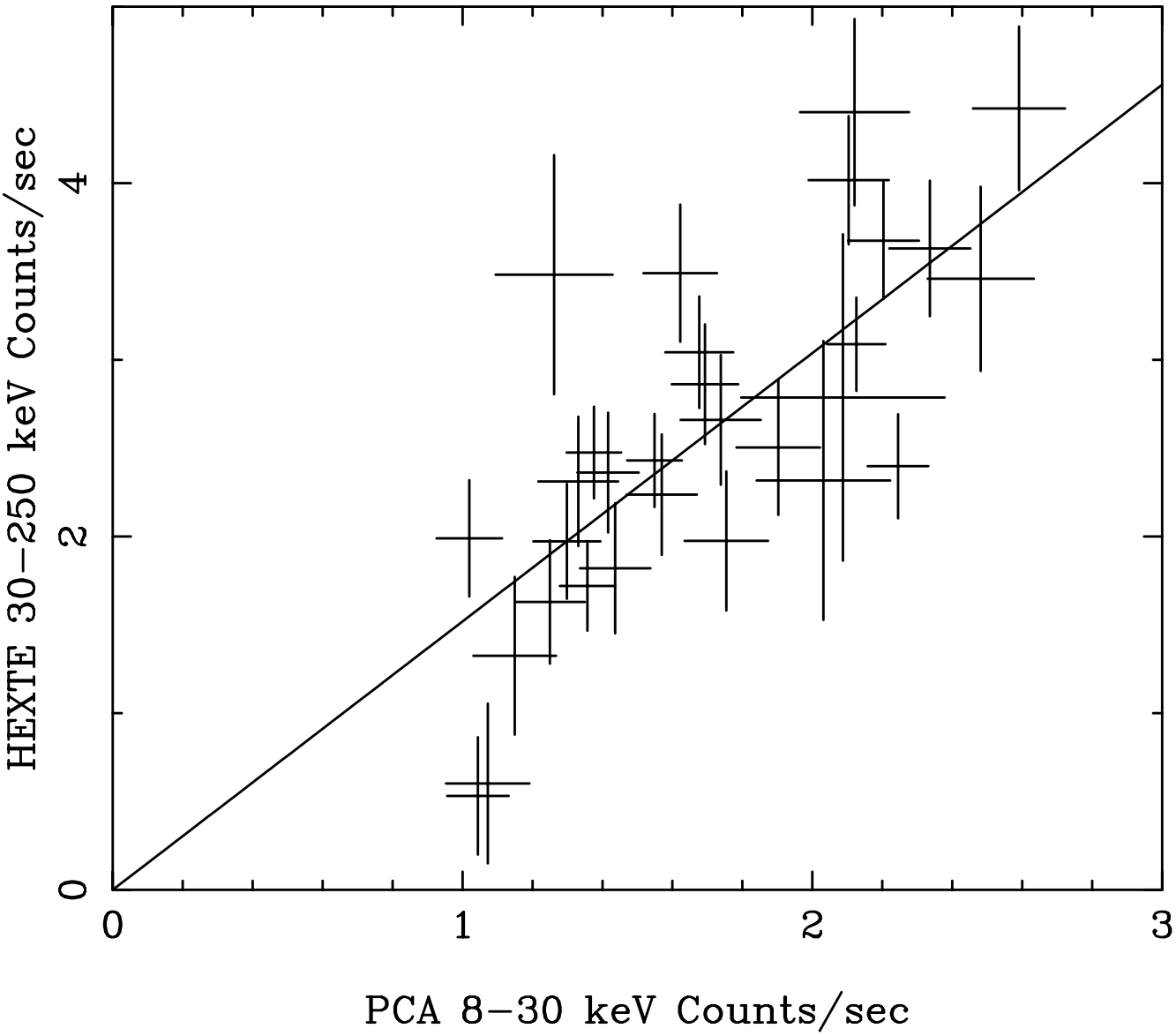

FIG. 3.— RXTE PCA 8 – 30 keV (channels 19 – 69) lightcurve versus the HEXTE 30 – 250 keV (channels 15 – 60) lightcurve, both binned on 4096 second intervals. The higher energy variability is completely consistent with the variability seen at lower energies.

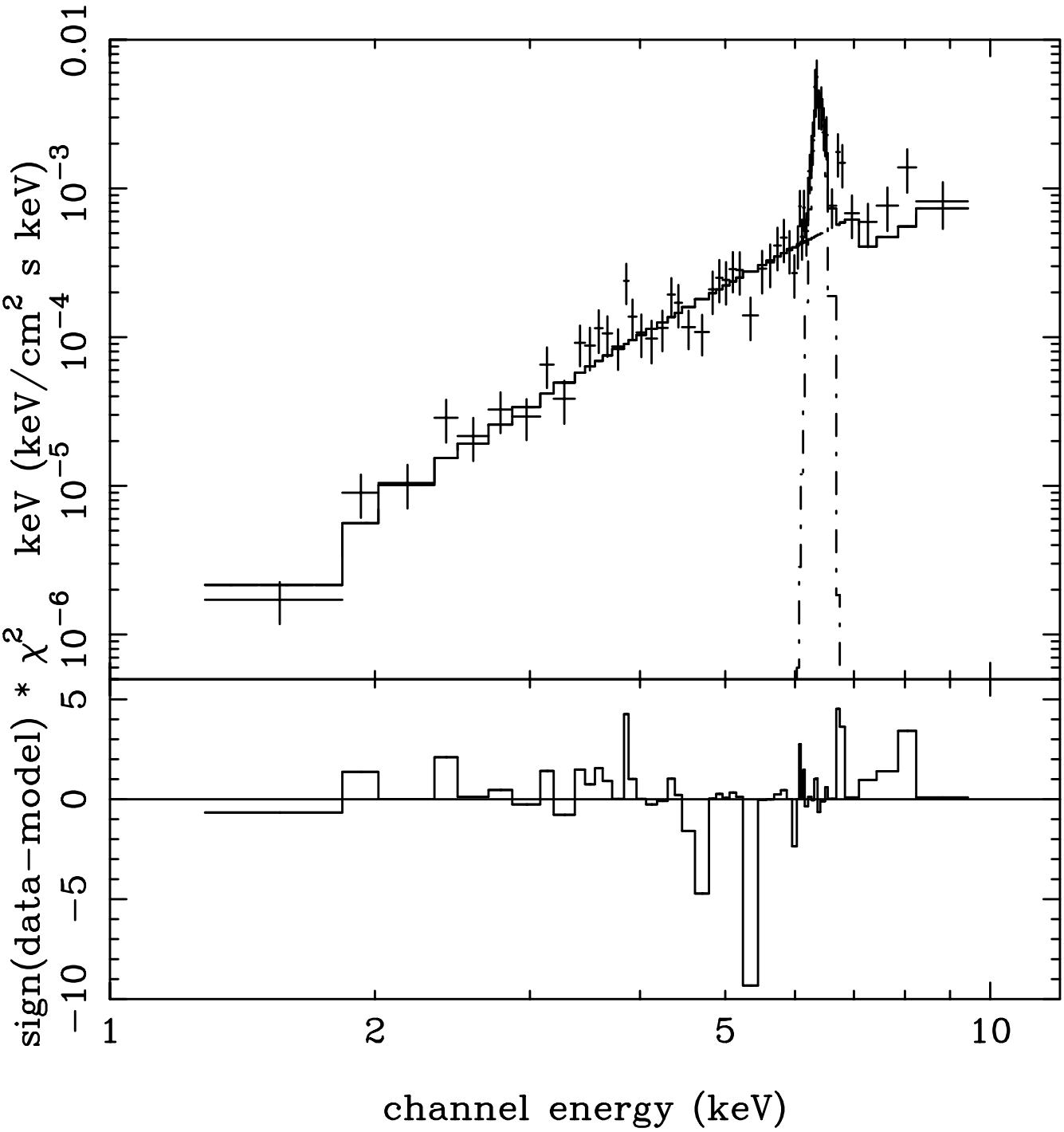

FIG. 4.— The upper panel shows the Chandra ACIS spectrum from the nucleus, deconvolved with the reflection model. Residuals to the fit are shown in the lower panel

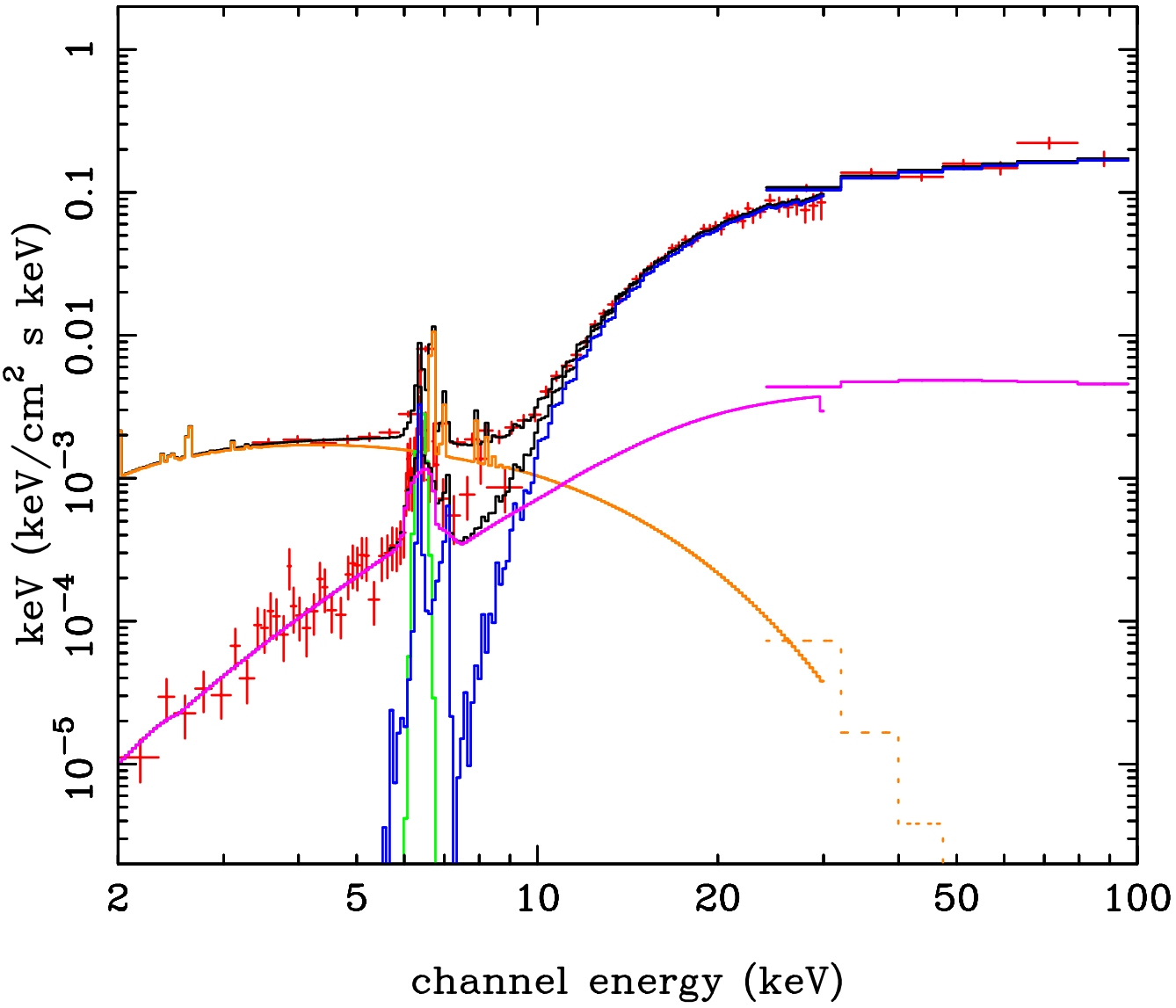

FIG. 5.— The total nuclear spectrum as seen by Chandra, PCA and HEXTE. The spectral data are unfolded from the instrument response using a model consisting of a heavily absorbed power law (blue) which dominates above 15 keV in the PCA and HEXTE data. Some fraction of the intrinsic (unabsorbed) spectrum is reflected from cold material (magenta) and escapes along a path which does not intercept the extreme obscuring material, dominating the *Chandra* emission. However, the wide field of view of the RXTE instruments means that the PCA spectrum includes both diffuse emission and off-axis sources. This additional X-ray flux is modelled by a hot plasma component which dominates the PCA data below $\sim$ 8 keV (orange), together with an emission line at 6.4 keV (green).

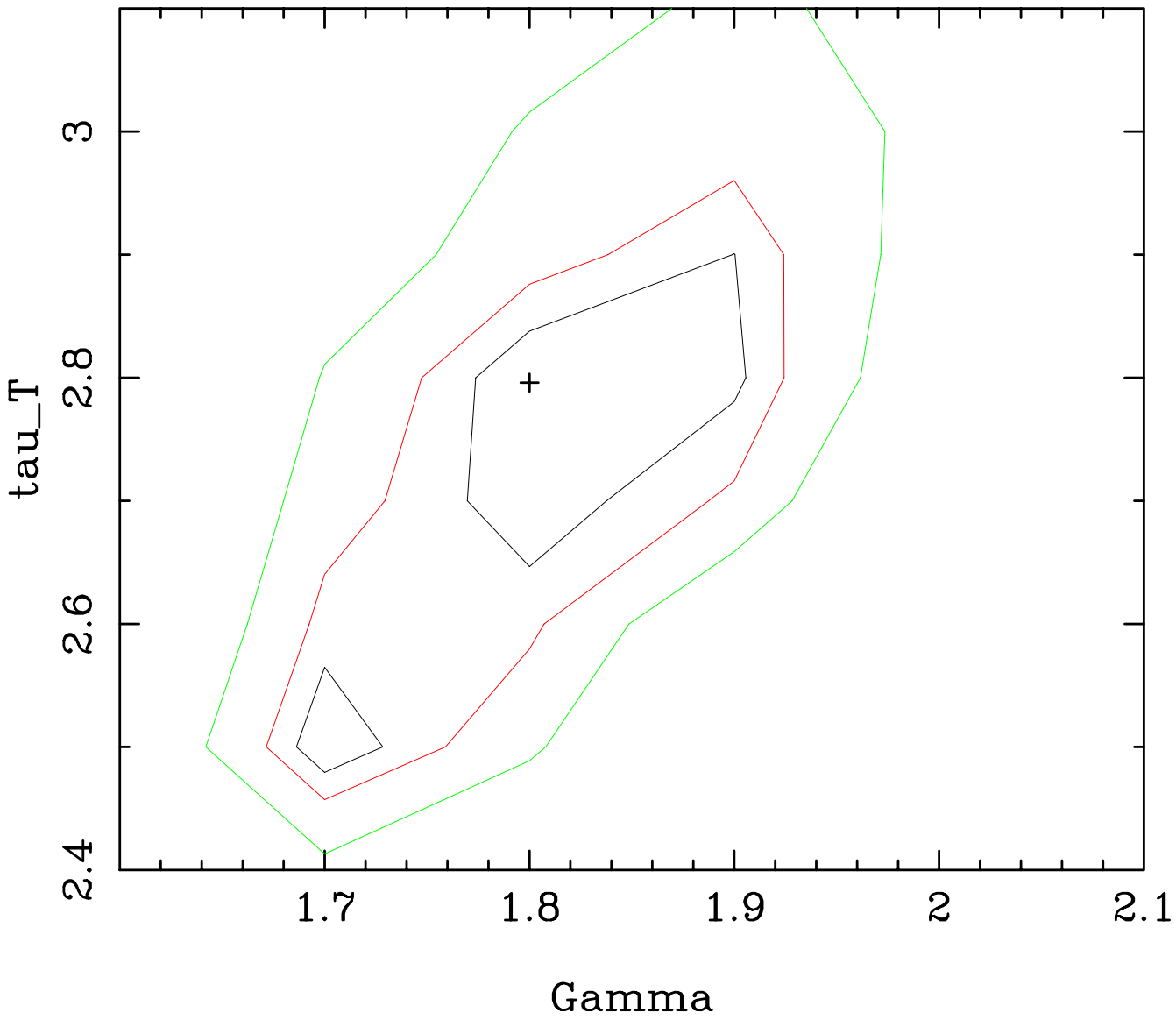

FIG. 6.— Confidence contours on the intrinsic spectral index versus the optical depth for the Monte Carlo absorption model shown in figure 5. This relates to the standard column density through $\tau = 1.21 \times 6.65 \times 10^{-25} N_H$

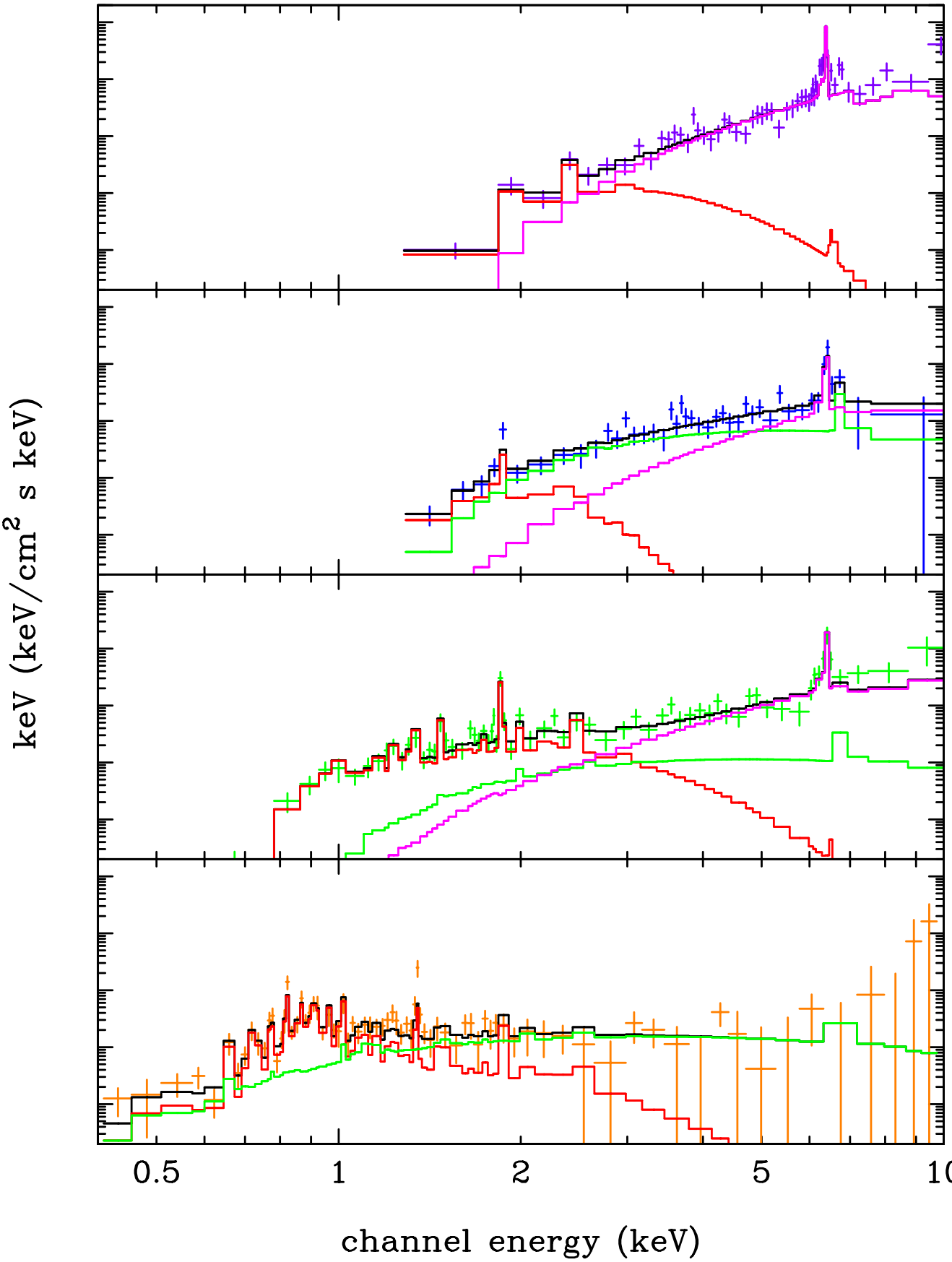

FIG. 7.— Unfolded spectral data from the Chandra image shown in Figure 1. The panels from top to bottom show the data from the nuclear region, `diff-nuc`, `diff-1` and `diff-2`, respectively. The model components are neutral reflection (magenta), a low temperature MEKAL plasma (red), and a high temperature MEKAL plasma (green).